Dynamic aspects of cerium dioxide sintering: HT-ESEM study of grain growth and pore elimination.

Renaud PODOR [#,*], Nicolas CLAVIER [#], Johann RAVAUX [#], Laurent CLAPAREDE [#], Nicolas DACHEUX [#] and Didier BERNACHE-ASSOLLANT°

[#] *Institut de Chimie Séparative de Marcoule, UMR 5257 CEA-CNRS-UM2-ENSCM, Site de Marcoule, Bat 426, BP 17171, F-30207 Bagnols sur Cèze Cedex*

°*ENSMSE, 158 Cours Fauriel, 42023 St-Etienne Cedex 2*

Tel : +33 4 66 33 92 02 / Fax : +33 4 66 79 76 11 / Email : renaud.podor@cea.fr

*** Corresponding author**

Running title: Dynamic aspects of CeO_2 sintering

Keywords: sintering, SEM, grain growth, ceramic, high temperature

Graphical abstract summary: Sintering of CeO_2 is studied by *in situ* high temperature scanning environmental microscopy (HT-ESEM) at T=1400°C. The morphological modifications of a single grains population are recorded for 6 hours. Kinetic parameters such as grain boundary velocities are extracted from the obtained image series. An intragranular surface pore elimination process is observed.

Graphical abstract: 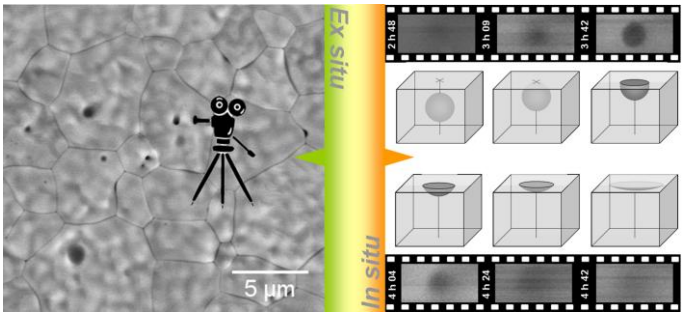

ABSTRACT

Sintering of CeO_2 is studied *in situ* by high temperature scanning environmental microscopy (HT-ESEM) at T=1400°C. The morphological modifications of a single grains population are recorded for 6 hours. Kinetic parameters are extracted from image series. The local grain growth determined from the single population studied *in situ* is compared to the general grain growth obtained by classical *ex situ* technique. Using HT-ESEM for sintering study is validated. The grain boundary velocities range between 0 and 5 $\mu m.h^{-1}$, with a mean value of about 1 $\mu m.h^{-1}$. The migration of the intragranular surface pores is described. Their velocities range between 0.4 and 1.2 $\mu m.h^{-1}$ and depend on pore diameters: the smaller the pore, the faster the pore velocity. The time required to fill a pore that arises at the sample surface are determined as a function of pore diameter. The time for pore elimination dependence with the pore diameters is also established.

1. **INTRODUCTION**

The final stage of sintering involves two major phenomena occurring simultaneously: pore shrinkage and grain growth. The microstructure evolution of a solid during sintering is then related to the kinetics of change in the grain size and pore distributions. These modifications are directly linked to atom and pore mobilities (and more generally to mass transfers) that generates displacements of grain boundary and pores[1,2]. Numerous models were developed to predict these processes but associated direct observations remained very rare. Indeed, even if the knowledge of experimental data is of great importance, only very few direct determinations of kinetic parameters are available, due to some difficulties to develop *in situ* observation methods that allow the visualisation of high temperature processes at the grain scale. Three main methods based upon recent technological developments have been used to observe *in situ* sintering process during heating :

- Transmission (and scanning transmission) electron microscopy [3-6] and associated imaging techniques (high resolution imaging [7,8], aberration-corrected high-angle annular dark-field – HAADF – detection [9]) which provide direct information at the atomic and nanometer grain scale.

- Synchrotron radiation X-ray computed tomography associated with *in situ* heating of the sample provides bulk material 3D imaging of samples [10,11].

- Scanning electron microscopy (SEM) that provides information at the grain scale with nanometer resolution. It was extensively used to observe sintered materials, but generally after sample cooling at room temperature [12-14] and surface preparation. The main problems linked to this technique are associated to the difficulty to perform successive analyses on materials at the same location.

One of the latest developments in electron microscopy is the environmental scanning electron microscope (ESEM) [15,16], which allows observing materials under a gaseous

atmosphere. Its association with specific attached devices offers the possibility to perform direct observations of native surfaces evolution with temperature or atmospheric pressure modifications [17]. *In situ* scanning electron microscope imaging of materials at high temperature is a challenging problem to which ESEM can bring interesting answers. Indeed, even if electron microscopes have been successfully adapted to observe the behaviour of materials at high temperature for long [18,19], the technological solutions developed limited the investigations to relatively low temperature experiments since heating materials above 1000°C generally results in the emission of infrared and visible light along with increased thermo-ionic emission of electrons [20]. This is the main limitation in obtaining ESEM images at high temperature (T > 1150°C). For example, Subramaniam [21] reports that the increase of electron emission with the temperature, results in poor signal to noise ratio on recorded images since a "white-out" effect is observed. The accompanying loss of contrast also results in poor image quality and loss of details. The degradation of imaging conditions becomes drastic as one approaches temperatures encountered in conventional ceramic sintering processes (T ~ 1300°C). Nevertheless, specific devices were recently designed to allow observations at very high temperatures : among them, a furnace was developed by Gregori et al. [20] to perform conventional SEM (under vacuum) *in situ* imaging at temperatures as high as 1450°C while Knowles and Hardt [22] designed a system coupled with a heat shield assembly reaching up to 1500°C (Figure 1). This system was used during this study.

The challenges of the present study are mainly to record HT-ESEM image series of oxide grains with a submicrometer resolution during 8 hours at T=1400°C in order to obtain new information on the sintering process of ceramic nanograins through the mathematical treatment of the obtained images. The selection of CeO_2 as model ceramic was motivated by its numerous applications such as its use as a surrogate for PuO_2 in the nuclear fuel industry

[23,24] as well as its potentialities within the framework of cathode materials in Solid Oxide Fuel Cells [25,26] which both requires the preparation of sintered components.

2. EXPERIMENTAL

2.1. Powder synthesis and characterization:

Powdered CeO_2 samples were obtained by firing cerium oxalate decahydrate, $Ce_2(C_2O_4)_3 . 10 H_2O$ at T=500°C for 6 hours [27]. This resulted in the formation of oxide nanopowders, constituted with 40-50 nm diameter aggregates (average crystallite size of 15 nm). The specific area of this powder, determined using a Micrometric ASAP 2020 apparatus under nitrogen atmosphere (BET method) was found about 47 ± 3 m^2g^{-1}. XRD patterns of the final oxides exhibited all the characteristic XRD lines of the FCC fluorite-type structure (space group $Fm\bar{3}m$) according to JCPDS file # 81-0792 [28].

2.2. Sample preparation:

Cylindrical pellets of 5 mm diameter were shaped by uniaxial pressure under 200 MPa at room temperature. About 1mm diameter part of the disc was considered to perform the HT-ESEM *in situ* experiments. The small size of the samples ensured a fast temperature homogenization of the studied piece of ceramic. Furthermore, the displacements of the sample coming from its sintering remained limited, avoiding the possibility of loosing the region of interest during analysis.

Complementary *ex situ* experiments were also performed at T=1300 and 1400°C. The density of the pellets sintered at T=1400°C were found typically close to 90 ± 2 % of the value calculated from crystallographic data.

2.3. HT-ESEM experiments:

In situ High Temperature Environmental Scanning Electron Microscopy (HT-ESEM) experiments were performed using a field emission gun environmental scanning electron microscope (model FEI QUANTA 200 ESEM FEG) equipped with a 1500°C hot stage. The water cooling system of this device was associated to an expansion tank that limited the stage vibrations during the experiment. The sample was directly placed in a 5 mm inner diameter MgO ceramic crucible covered with platinum paint. When the specimen was placed in the hot stage, the chamber was evacuated then filled with the adequate gaz.

During this work, the observations were performed under water vapour at an operating pressure of 120 Pa and a specific detector was used for *in situ* gaseous secondary electron imaging at high temperature. The oxygen pressure in the ESEM chamber was not measured but was estimated between a maximum value of 25Pa (by considering that the chamber was filled by 120Pa of air) and a minimum value of 10^{-3} Pa. Indeed, water vapour was produced in the ESEM chamber from a water bath maintained at T = 25°C : in these conditions, the quantity of oxygen solubilised in water was approximately 8 $mg.L^{-1}$ [29].

The sample was heated at 30°C.min^{-1} up to 1400°C then maintained isothermally at this temperature in the ESEM chamber all along the experiment. Micrographs were recorded at regular intervals during the heat treatment of the sample on a selected part of the ceramic with different magnifications. The furnace temperature was controlled by a thermocouple placed near the MgO crucible. The sample temperature accuracy was verified during each experiment by checking the fusion temperature of a small gold wire.

In order to overcome the problems described in the introduction (mainly the loss of electronic contrast associated with the electronic emission of the black body which both increased with increasing temperature) and to enhance the electronic emissions carrying

information (i.e. secondary electrons and back-scattered electrons the accelerating voltage was increased to 30kV. Similarly, the current of the electron beam was maximized: the spot size was then adjusted to its higher value and the intermediate diaphragm was removed. Increasing the current led to a decrease of the resolution of the obtained images. Finally, controlling the gas pressure in the SEM chamber allowed a precise adjustment of the image contrast and brightness. The "heat shield bias", "sample bias" and image focus were also adjusted for each image recording to get a sharp and stable image.

A typical HT-ESEM image recorded during this study is reported in Figure **2**a. The quality of the obtained images obtained at 1400°C was good enough to extract basic data (such as grain size, pore size and location, …) that were used for further kinetic parameter determination. It must be noted that information are local and representative of a small grain size population (30-200 grains, depending on the heating time).

3. RESULTS AND DISCUSSIONS

3.1. Validation of the HT-ESEM use for direct study of grain growth

The image obtained from the HT-ESEM *in situ* observation of the samples heated at 1400°C (Figure **2**a) was compared to an image recorded on a sample heated *ex situ* at 1400°C for the same run duration (Figure **2**b) (no specific metallographic preparation was performed on the sample which surface was observed without any carbon deposition). Both samples present the same general shapes, with well defined grain boundaries and the presence of intergranular and intragranular pores.

On this basis, the local sintering stop observed by Popma [30] when focusing the electron beam ion on ZrO_2 nanolayers was not evidenced in our study. Indeed, the local

sintering on sample surface zones that were not observed (*i.e.* exposed to the electron beam) was identical to the local sintering determined on the observed zone.

A statistical study of the mean grain size evolution was also performed from the 25µm × 25µm area images recorded *in situ*. Grain areas and perimeters were thus extracted though mathematical treatment of images using the ImageJ software[31] then the main grain size diameters were determined assuming that the grains exhibited a spherical geometry. The obtained data are reported in Figure 3 as a function of run duration for two temperatures (T=1300°C and 1400°C) and compared to the grain size distributions determined by the "classical" *ex situ* technique, for 3 heating durations as well as to results reported in the literature[32]. Both sets of data fit well together meaning that the grain growth kinetics determined at the "grain scale" (HT-ESEM *in situ* experiments) is of the same order of magnitude than the data obtained at the "sample scale" (classical *ex situ* experiments). The global grain size differences noted between T=1300°C and 1400°C indicates that an important temperature effect was evidenced by HT-ESEM technique. The main conclusion was that the phenomena described from HT-ESEM images were representative of the sample surface sintering behaviour at the experimental temperature. A forthcoming paper will be specifically dedicated to the effect of temperature on grain growth kinetics.

3.2. Study of local kinetic processes

A series of selected HT-ESEM images corresponding to different heating duration at T=1400°C are reported in Figure 4. As illustrated by this series, the main interest of the use of the HT-ESEM technique lied in the possibility to observe directly the local morphological modifications, i.e. at the grain scale, with an approximately 10 nm resolution. The morphological changes occurring on one population of the grains are related to grain size, grain boundary and (inter- and intra-granular) porosity that were observed *versus* the heating

time. As a consequence, kinetic parameters listed below (then described separately) were determined by numerical treatment performed on the images:

a. determination of grain areas and perimeters at the surface of the sample that led to the local grain growth kinetics;
b. measurement of the distance between two grain boundaries that allowed determining the grain boundary velocity;
c. treatment of images on local intra-granular surface pores that allowed performing measurements on intra-granular porosity velocity and lifetimes.

3.2.1. Local grain growth kinetics

The grain sizes, expressed as grain diameters (calculated from the grain area evaluated by observation of the sample surface), were determined for each grain observed in Figure 4 and reported in Figure 5 as a function of heating time. The single grain behaviour appeared to be erratic compared to the average grain behaviour since some grains reached the sample surface while others fully merged with their neighbours. This behaviour was directly linked to the mass transfers occurring due to the curvature of grain boundaries. Indeed, if the starting powder was composed by grains of different sizes, which is usually the case, the curvature of the boundary between two grains induced simultaneously a compression in the smallest grain and a tension of the matter inside the biggest one [33,34]. The constraint gradient generated from this difference then led to the establishment of diffusion processes from the small to the big grains. This phenomenon, close to Ostwald ripening, is responsible for the progressive disappearance in the smallest grain population of the samples during sintering [35,36].

In the present case, the consequence of such diffusion processes was directly observed *in situ* through the variation of individual grain sizes and the displacement of grain boundaries to the centre of curvature of the smallest ones.

3.2.2. Velocity of the grain boundaries

The mass transfer from one grain to its neighbours occurs through the grain boundary. In this case, the grain size modifications imply variations in the grain frontiers and directly control the velocity of the grain boundaries. Since scanning electron microscope allows recording two-dimensional images of the sample surface, the grain boundaries are represented as segments separating two grains. Their movements then reflect the displacement of the plane separating two grains. As it was not possible to keep an immobile reference in the present case, the velocity of the grain boundaries was determined from the $\Delta L/\Delta t$ ratio, where ΔL was the distance difference between two opposite grains boundaries (Figure 6a) referring to two successive images and Δt the associated time difference. The obtained values (Figure 6b) were in the range 0 to 5 $\mu m.h^{-1}$. Such variations in the instantaneous velocity of the grain boundaries with time indicated that the displacement of the grain boundaries accelerated or decelerated very quickly.

If one considers the behaviour of a single grain, the size of this grain can increase at a given time, stabilize then finally decrease, depending on the geometry of the system. Indeed, the displacement of grain boundaries not only depends on the grain sizes but also on the number of neighbours. This latter implies a variation of the dihedral angle formed between the boundaries of a same grain such as for 6 neighbours, the dihedral angle barely equals 120° leading to plane interfaces which stabilize the grain while it growths above 6 neighbours and shrinks below [2]. In these conditions, the evolution of the solid matrix occurring during the sintering process could lead to important modifications in the environment of a single grain, leading this latter to adopt different behaviours during the heat treatment. The associated displacement of the grain boundaries was thus positive or negative, relatively to the grain centre.

Also, the velocity of the grain boundaries strongly varied from one grain boundary to another within the same single grain (Figure 6b). This implies that the mass transfer was favoured through specific grains boundaries. This is in good agreement with theoretical models that link the grain boundary velocity (and the associated mass transfer) to the curvature of the grain boundary (and differences between local surface tensions that is the driving force of mass transfers) [33,34].

The grain boundary velocity distribution is reported in Figure 7. In this representation, the velocities are reported as absolute values. The distribution was centred on 0-0.5 $\mu m.h^{-1}$ family and the average value determined from a set of 72 data was about 1 $\mu m.h^{-1}$. This indicates that some grains were locally stabilized for long periods while other zones of the sample (not far from the immobile grain) were strongly modified. The maximum rate determined reached 5 $\mu m.h^{-1}$ and corresponded to an important local rearrangement (elimination of a grain in the present case).

3.2.3. Velocity of intragranular porosity

Intragranular pores were also clearly visible on the HT-ESEM images reported in Figure 4. The presence of intragranular pores up to 3 µm was reported by Argoitia [32] for CeO_2 sintering at T=1400°C as a consequence of pores detachment from grain boundaries. A zoom of the zone examined is reported in Figure 8a. As this technique allowed the observation of surface phenomena (classically only few nanometres in depth contribute to the image formation), the porosity observed corresponded to open or closed porosity that was located close to the grain surface. Nevertheless, in the present case, the electron beam properties and the environmental electron detection mode *via* the gaseous secondary electron detector favoured the under-surface scanning up to a depth that depends on the acceleration voltage and on the sample density. Indeed, the 30 kV incident electron beam interacts with CeO_2

($\rho = 7.215$ g.cm^{-3}) up to 3.5 µm depth in the material. Even if secondary electrons are emitted at the extreme surface of the sample, backscattered electrons can allow screening the material up to approximately 500 nm in depth. As the signal collected using the detector associated with the HT device comes from both secondary and backscattered electron emissions, the intra-granular pores can be observed even if they do not emerge (but arise) at the surface of the grain.

If the pore moved to the surface and emerged, its displacement was observed and related to a modification in the image of the pore (Figure 8b). Mathematical treatment performed on the image series allowed the reconstruction of the pore trajectory inside the solid. The extraction of the grey-level curves using ImageJ software was performed on each image of the series along a line which went through the pore diameter (Figure 8c). The obtained curves were then interpreted regarding to the pore position relatively to the sample surface. The pore was considered to arise up its half-size when the grey-level curve exhibited the smallest width (Figure 8c) and the highest intensity at the centre (see Figure 8a and d, t=3h42). The pore velocity was determined by assuming that the pore was just reaching the surface when its image began focusing. Hence, it was displaced from a distance corresponding to its radius between the time corresponding to the observation of the first focussed image and the time when the image corresponded to its full diameter. The pore velocity was then determined from the pore radius and the elapsed time between the recordings of both images.

The driving force for the pore displacement was probably the curvature difference between the front side and the back side of the pore. This is true in the case of inter granular porosity when the pores morphology is modified by the grain boundary displacements. On the contrary, if one considers intra granular porosity, the pores were supposed to be perfect spheres if the superficial tension was isotropic in the solid around the pore. In this case, the

driving force for the pore displacement should be linked to gradients from the bulk to the surface, due to temperature, Ce/O stoichiometry (in CeO_{2-x}) or anisotropic pressure in the matrix around porosity. Such anisotropy was effective in grains located close to the sample surface as already described by Lange in composites [37].

The pore velocities determined for 14 pores with different diameters are gathered in Figure 9 *versus* the pore diameter. The error bars reported in this figure were mainly dependent on the number of images recorded. Indeed, the minimum time between two micrographs recordings reached approximately 2 minutes. As a consequence, if the pore arised at the sample surface in a time lower than 2 minutes, this phenomenon was not observed. It corresponded approximately to an observable pore size limit of 200 nm.

The pore velocities determined from the images analysis ranged between 0.4 and 1.2µm.h^{-1} and clearly depended on the pore size. Indeed, two behaviours were distinguished: above a size of 500 nm, the pore velocities were typically limited to about 0.5 µm.h^{-1} while they reached more than 1 µm.h^{-1} for pore diameters below 400 nm. This result confirmed that the smaller the pore diameter, the higher the pore velocity which is in good agreement with the general laws for the pore displacement description reported by Nichols [38] and Bernache-Assollant [36]. These latter rely the pore mobility with the mechanisms that control their displacement as a function of k/r^2, k'/r^3 or k''/r^4 corresponding to superficial diffusion, gaseous diffusion, evaporation-condensation or volume diffusion, respectively (where k, k' and k" are constants and r is the radius of the pore) [39].

3.2.4. Elimination of intragranular porosity at the sample surface

After the intragranular pore emerged up to its half-height, the apparent pore diameter increased and its depth decreased with heating time (Figure 8d). During this period, the pore

was at the sample surface and progressively filled in according to a mechanism probably close to that described by Drory and Evans [40], *i.e.* surface diffusion mechanism. The apparent diameter of the pore increased because of some mass transfer from the border of the pore to its centre. The time required for elimination of intra-granular porosity was equal to the elapsed time between the observation of the full pore diameter and its complete disappearance. This parameter, called pore filling time, was determined for 24 pores (Figure 10). It increased from 12 to 120 minutes with increasing pore size. This was directly linked to the mass transfer required to close the hole corresponding to the pore arising at the sample surface.

This type of intragranular surface pore elimination process was never determined directly from *ex situ* images. However, when looking at *ex situ* images recorded at T=1400°C (Figure 2b), few intragranular pores were observed, each one being at a particular stage of the pore elimination process. Thus, this surface pore elimination process is relative to pores that are initially close to the sample surface (surface pores) and cannot be extended to the bulk porosity. Furthermore, the pore elimination process was described for intragranular porosity due to the spherical geometry of these pores that allows determining pore velocities and lifetimes, but it can be also described for intergranular surface pores.

It must be noted that during this study, no pore breakaway from the grain boundaries was observed on the recorded image series - but this does not exclude the possibility for such a phenomenon to occur in the bulk or during earlier stages of sintering. Furthermore, no formation of intragranular surface pores was directly observed through a mechanism involving the separation of pores from the boundaries of disappearring grains, such as reported by Sakarcan et al. [12] during the study of pore breakaway in MgO ceramics at T=1500°C. On the contrary, some intragranular pores seemed to be caught up by the grain

boundaries (see Figure 4). These observations can be attributed to the fact that the observed phenomenons are related to the sample surface.

4. CONCLUSIONS

The importance of the use of HT-ESEM for the study of sintering and grain growth in ceramics was clearly evidenced in this study. This technique allowed the direct observation of phenomena at the micrometer scale with a 10 nanometer resolution, for long durations at high temperature (up to 6 hours at T=1400°C). This experimental method could be applied to various type of materials (oxides, sulphates, phosphates, metals…), depending on their reactivity in the ESEM chamber with gases or ceramics.

In the studied CeO_2 materials, the sample morphology (grain size and presence of inter and intra granular pores) obtained after *in situ* heating in the HT-ESEM was identical to that obtained during *ex situ* experiments. Through the analysis of sample images recorded at different run durations, it was possible to precisely determine kinetic parameters such as grain growth, grain boundaries velocities and pore elimination rates.

Intragranular surface pore migration from the bulk to the sample surface as well as surface elimination of the intragranular pores was described. Intergranular surface pore velocities were also determined. Such data were only determined using *in situ* investigation techniques.

Finally, the main conclusion of the present study was that, even if the comprehension of sintering lied for long on theoretical models based upon the observation of samples cooled down from high temperature, direct *in situ* observations at the nanometer scale of the sintering - and grain growth - processes yielded to the same conclusions. The strength of the *in situ* HT-ESEM technique lies in the possibility of quantifying local physical properties of grain boundaries or pores that can not be directly assessed by other classical methods.

ACKNOWLEDGMENT

The authors would like to thank the MATINEX French Research Group (Innovative materials in extreme conditions, CEA / CNRS / AREVA / EDF / French Universities) included in the PACEN Program for its financial support. This work was also funded thanks to the support of Agence Nationale de la Recherche (ANR-08-BLAN-0216).

References

1. Ding L, Davidchack RL, Pan J. A molecular dynamics study of sintering between nanoparticles. *Comp Mater Sci* 2009;**45**:247-56.

2. Kang SJL. *Sintering*. Oxford: Elsevier Butterworth-Heinemann; 2005.

3. Rankin J, Sheldon BW. In situ TEM sintering of nano-sized ZrO_2 particles. *Mat Sci Eng A* 1995;**204**:48-53.

4. Theissmann R, Fendrich M, Zinetullin R, Guenther G, Schierning G, Wolf DE. Crystallographic reorientation and nanoparticle coalescence. *Phys Rev B* 2008;**78**:205413.

5. Holland TB, Thron AM, Bonifacio CS, Mukherjee AK, van Benthem K. Field assisted sintering of nickel nanoparticles during in situ transmission electron microscopy. *Appl Phys Lett* 2010;**96**:243106.

6. Chen Y, Palmer RE, Wilcoxon JP. Sintering of passivated gold nanoparticles under the Electron Beam. *Langmuir* 2006;**22**:2851-5.

7. Zhang WJ, Miser DEJ. Coalescence of oxide nanoparticles: In situ HRTEM observation. *Nanopart Res* 2006;**8**:1027-32.

8. Zink N, Therese HA, Pansiot J, Yella A, Banhart F, Tremel W. In situ heating TEM study of onion-like WS_2 ans MoS_2 nanostructures obtained via MOCVD. *Chem Mater* 2008;**20**:65-71.

9. Asoro MA, Kovar D, Shao-Horn Y, Allard LF, Ferreira PJ. Coalescence and sintering of Pt nanoparticles: in situ observation by aberration-corrected HAADF STEM. *Nanotechnology* 2010;**21**:025701.

10. Nöthe M, Schultze M, Grupp R, Kieback B, Haibel A, Banhart J. Analysis of particle rearrangement during sintering by micro focus computed tomography (µCT). *Mat Sci Forum* 2007;**534-536**:493-6.

11. Kieback B, Nöthe M, Banhart J, Grupp R. Investigation of Sintering Processes by Tomography. *Mater Sci Forum* 2010;**638-642**:2511-6.

12. Sakarcan M, Hsueh CH, Evans AG. Experimental assessment of pore breakaway during sintering. *J Am Ceram Soc* 1983;**66(6)**:456-61.

13. Maître A, Beyssen D, Podor R. Effect of ZrO_2 additions on sintering of SnO_2-based ceramics. *J Eur Ceram Soc* 2004;**24**:3111-8.

14. Yang KC, Shen P, Gan D. On the reorientation of $ZrTiO_4$ particles during reactive sintering of TiO_2–ZrO_2. *J Eur Ceram Soc* 2008;**28**:1169-76.

15. Danilatos GD. Introduction to the ESEM instrument. *Microsc Res Technique* 1993;**25**:354-61.

16. Johnson R. Environmental scanning electron microscopy. An introduction to ESEM. Philips, Eindhoven: Robert Johnson associates; 1996.

17. Donald AM. The use of environmental scanning electron microscopy for imaging wet and insulating materials. *Nat Mater* 2003;**2**:511-6.

18. Biswas DR, Nath DKJ. Direct observation of sintering of VAD soot particles by hot stage scanning electron microscopy. *Mater Sci Lett* 1983;**2**:245-8.

19. Erhart H, Wang R, Rapp RA. In situ SEM study of the high-temperature oxidation of an Fe-Mn-Al-Si alloy. *Oxid Met* 1984;**21**:81-8.

20. Gregori G, Kleebe HJ, Siegelin F, Ziegle G. In situ SEM imaging at temperatures as high as 1450°C. *J Electron Microsc* 2002;**51**:347-52.

21. Subramaniam S. In situ high temperature environmental scanning electron microscopic investigation of sintering behavior in barium titanate. PhD thesis. Cincinnati, USA: University of Cincinnati; 2006.
PhD thesis, University of Cincinnati, Cincinnati USA; 2006.

22. Knowles RW, Hardt TA. High temperature specimen stage and detector for an environmental scanning electron microscope. European Patent EP 1 003 200 B1 (1996)

23. Tyagi AK, Ambekar BR, Mathews MD. Simulation of lattice thermal expansion behaviour of $Th_{1-x}Pu_xO_2$ ($0.0 \leq x \leq 1.0$) using CeO_2 as a surrogate material for PuO_2. *J Alloy Compd* 2002;**337(1-2)**:277-81.

24. Kim HS, Joung CY, Lee BH, Oh JY, Koo HY, Heimgartner P. Applicability of CeO_2 as a surrogate for PuO_2 in a MOX fuel development. *J Nucl Mater* 2008:**378(1)**:98-104.

25. Tuller H, Nowick AS. Defect structure and electrical properties of nonstoichiometric CeO_2 single-crystals. *J Electrochem Soc* 1979;**126(2)**:209-17.

26. Eguchi K, Setoguchi T, Inoue T, Arai H. Electrical properties of ceria-based oxides and their applications to solid oxide fuel cells. *Solid State Ionics* 1992;**52**:165-72.

27. Elhoute S, Ali ME. Thermal decomposition of cerium oxalate and mixed cerium-gadolinium oxalates. J Therm Anal 1991;37:907-13.

28. Wolcyrz M, Kepinski L. Rietveld refinement of the structure of CeOCl formed in Pd/CeO_2 catalyst – Note on the existence of a stabilized tetragonal phase of La_2O_3 in La-Pd-O system. *J Solid State Chem* 1992;**99**:409-13.

29. Air solubility in water. http://www.engineeringtoolbox.com/airsolubility-water-d_639.html.

30. Popma RLW. Sintering characteristics of nano-ceramics, PhD thesis, University of Groningen; 2002.

31. Rasband W. ImageJ software, Image processing and analysis in Java, http://rsbweb.nih.gov/ij/

32. Argoitia A. Elaboration et propriétés de céramiques à base d'oxyde de cérium. PhD Thesis, Université de Limoges, Limoges France; 1989.

33. Kellett BJ, Lange FF. Thermodynamics of densification – 1. Sintering of simple particle arrays, equilibrium-configurations, pore stability and shrinkage. *J Am Ceram Soc* 1989;**72**:725-34.

34. Lange FF, Kellett BJ. Thermodynamics of densification – 2. Grain growth in porous compacts and relation to densification. *J Am Ceram Soc* 1989;**72**:735-41.

35. Lifschitz IM, Slyosov VV. The kinetics of precipitation from supersaturated solid solutions. *J Phys Chem Solids* 1961;**19**:35-50.

36. Bernache-Assollant D. Chimie-Physique du frittage. Forceram (Hermes); 1993.

37. Lange FF, Metcalf M. Processing-related fracture origins 2. Agglomerate motion and cracklike internal caused by differential sintering. *J Am Ceram Soc* 1983;**66(6)**:398-406.

38. Nichols FA. Kinetics of diffusional motion of pores in solids. *J Nucl Mater* 1969;**30**:143-65.

39. Herring C. Effect of change of scale on sintering phenomena. *J Appl Phys* 1950;**21**:301-3.

40. Drory MD, Evans AG. Elimination of surface voids in ceramics. *J Am Ceram Soc* 1985;**68(6)**:342-8.

Figures :

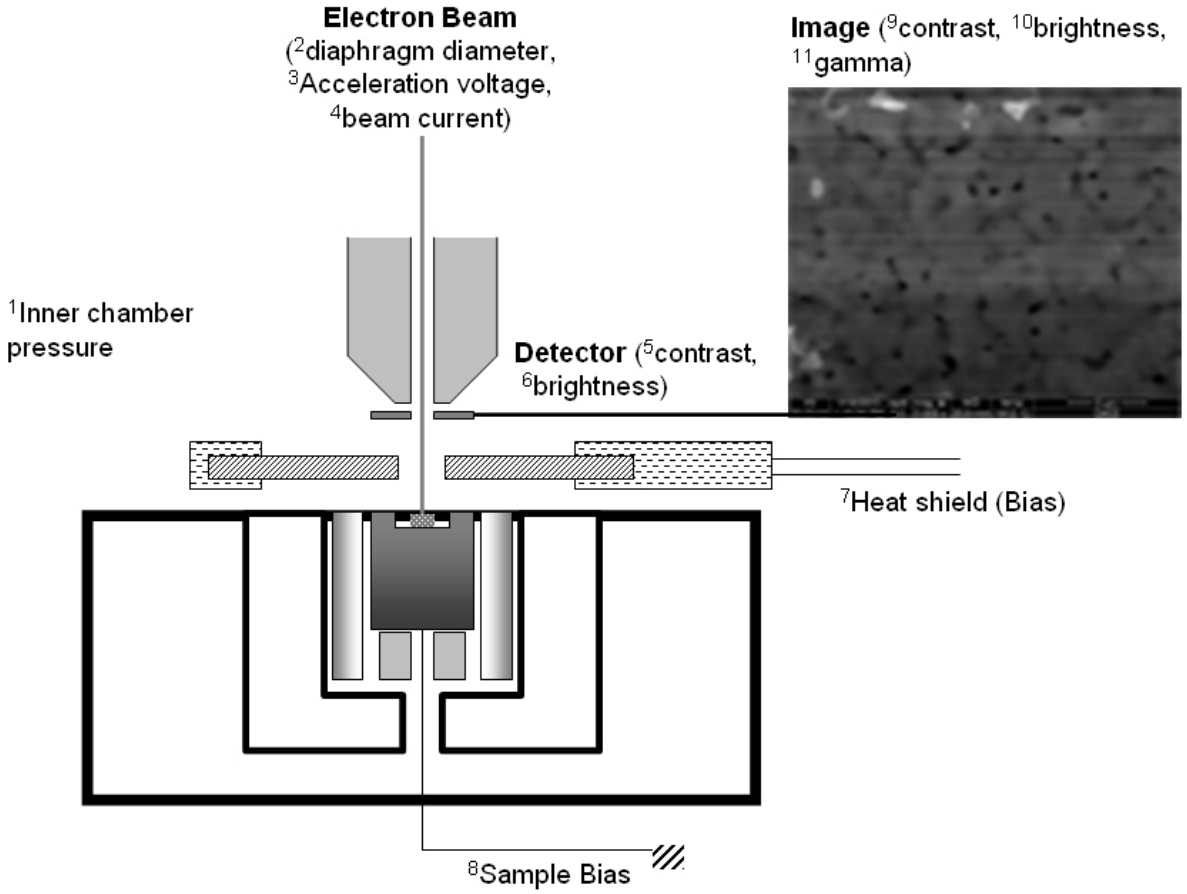

Figure 1 – Scheme for the use of the HT-ESEM with all possible image condition adjustments.

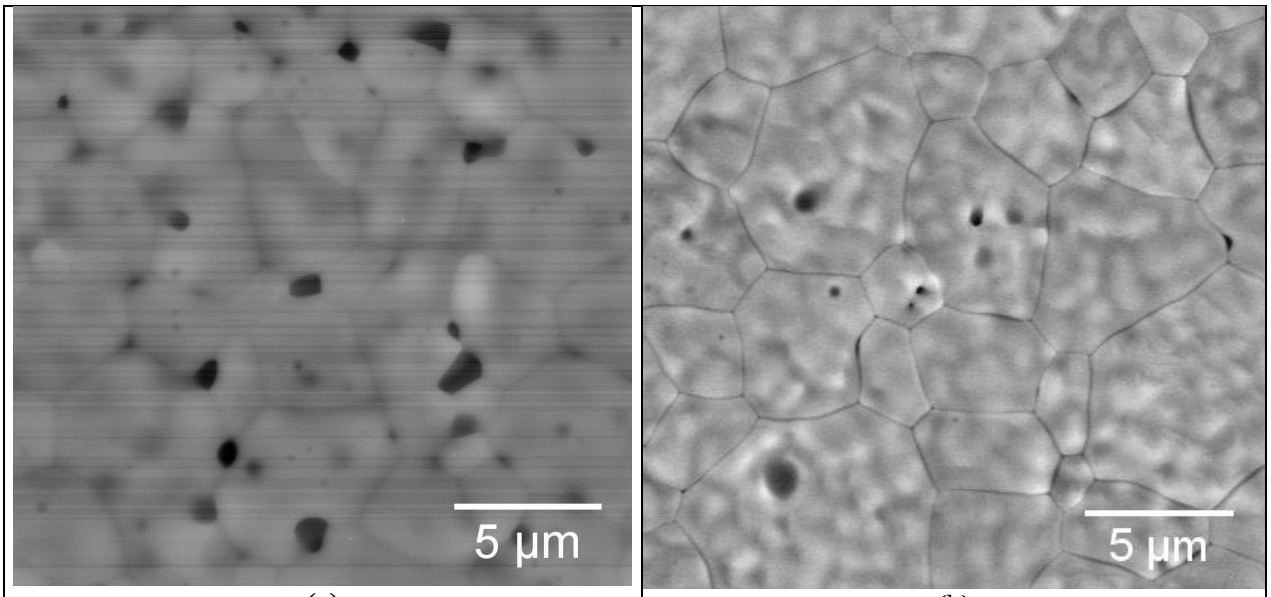

(a) (b)

Figure 2 – (a) Typical HT-ESEM image recorded at T=1400°C, after 2.5 hours heat treatment of a CeO_2 sample. (b) Typical image recorded for a CeO_2 sample heated for 2.5 hours at T=1400°C in a furnace then cooling at room temperature.

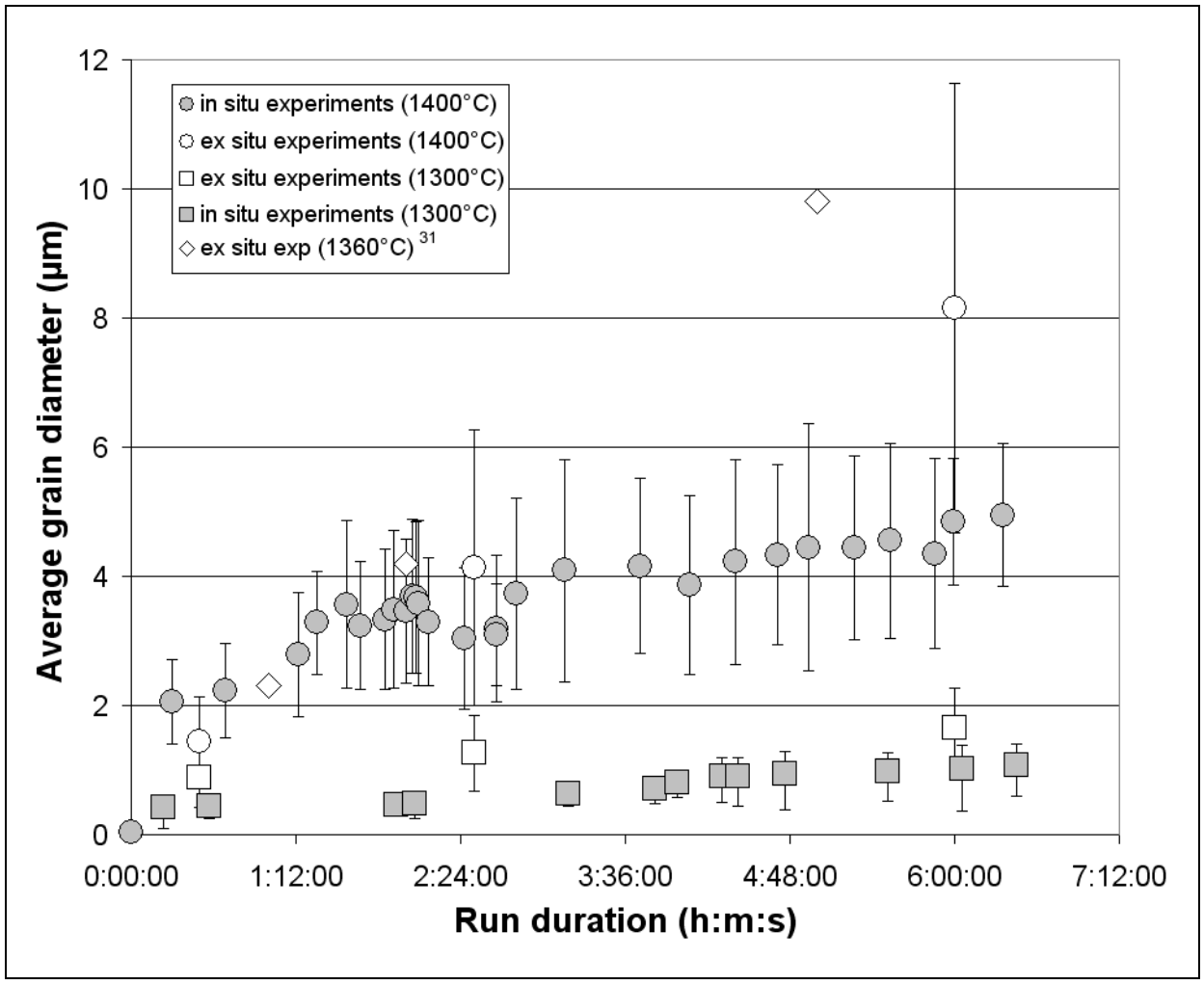

Figure 3 – Average grain size determined at 1300°C and at 1400°C from 25µm × 25µm HT-ESEM images for *in situ* and *ex situ* data (this study and from Argoitia [32]).

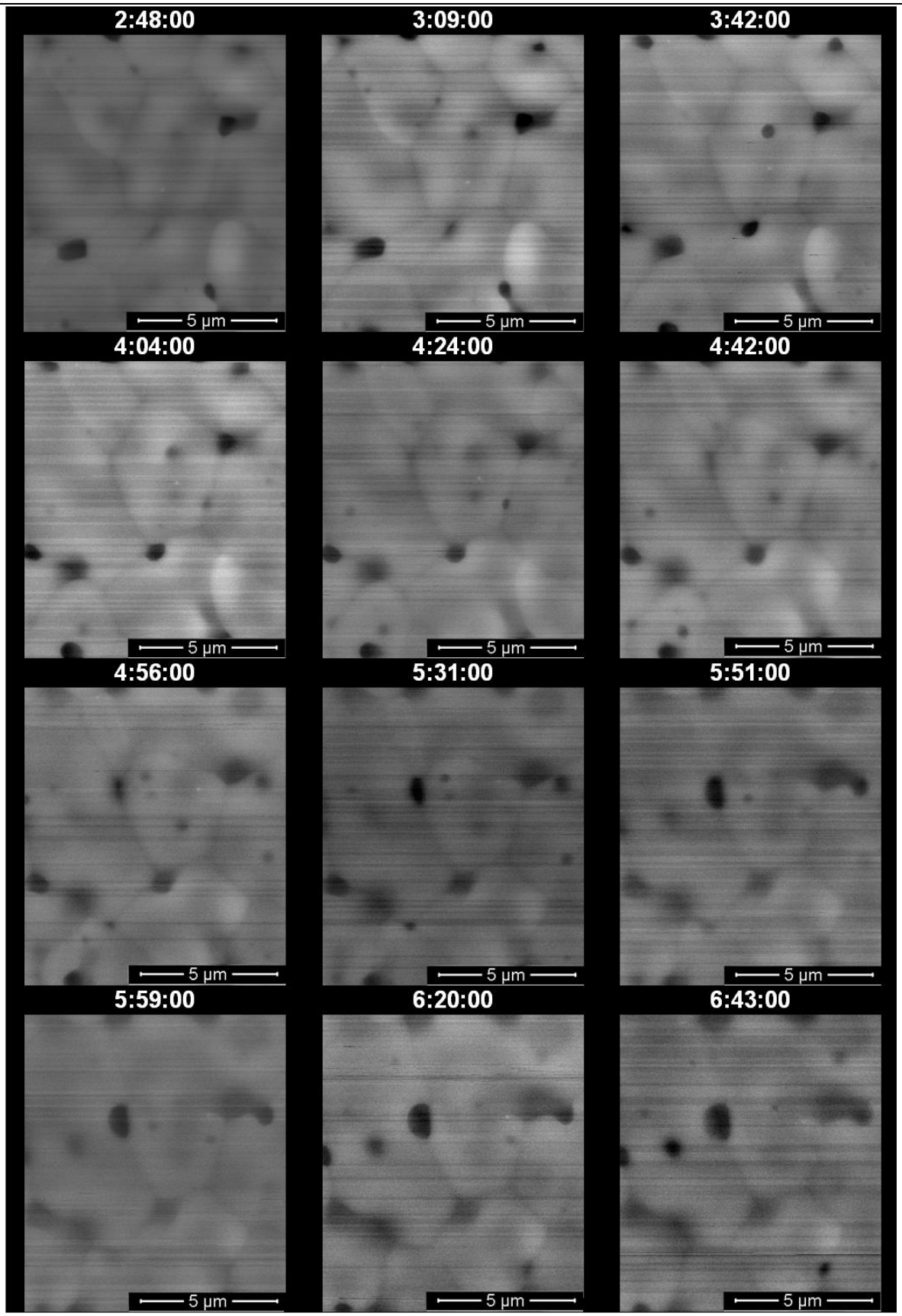

Figure 4 – Selected HT-ESEM images corresponding to different holding times at T=1400°C (heating durations are expressed in h:mn:s). (Please see additional video data for movie)

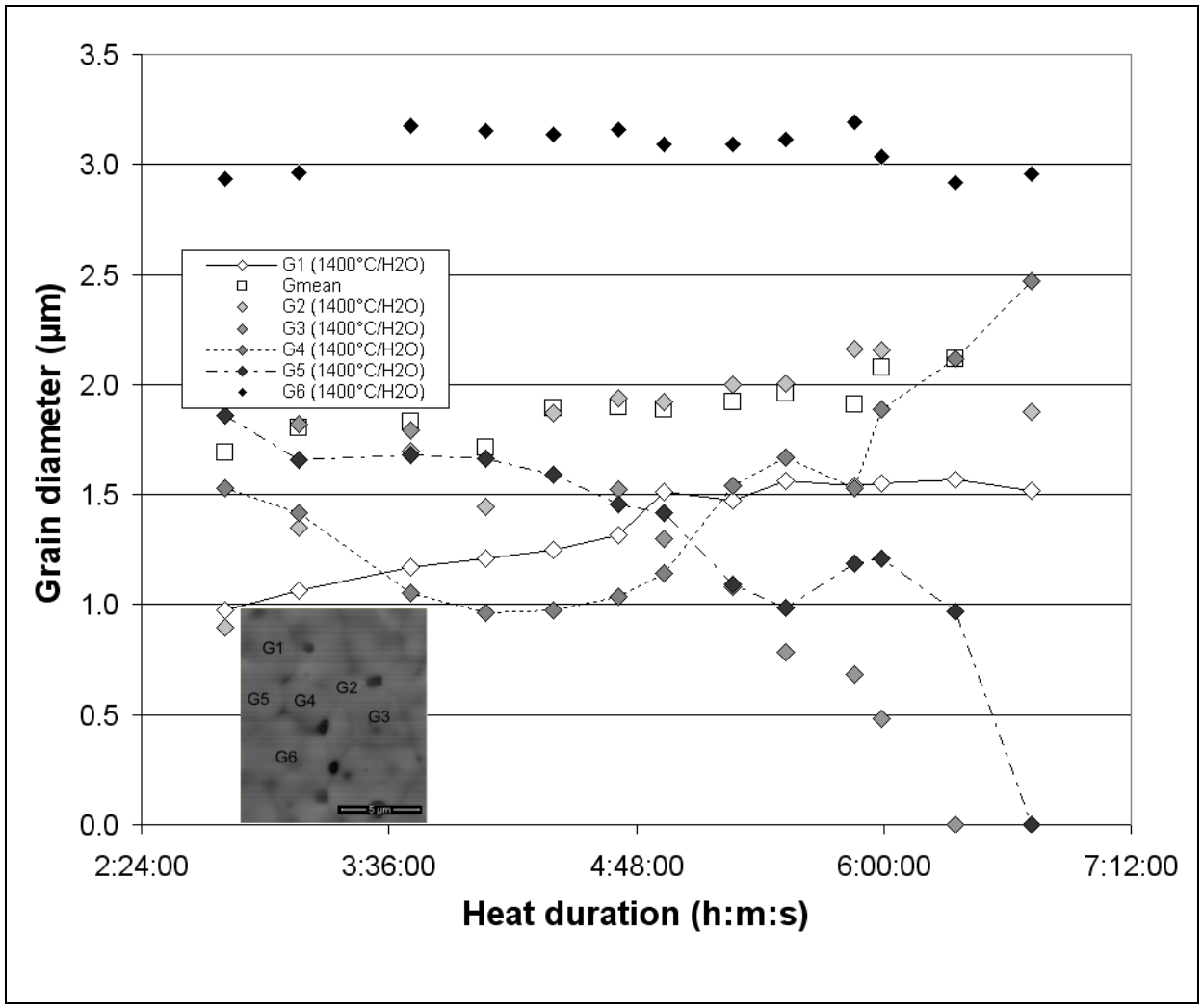

Figure 5 – Variations of local grain sizes *versus* of heating duration. Locations of the studied grains at the surface of the sample are reported on the inserted image.

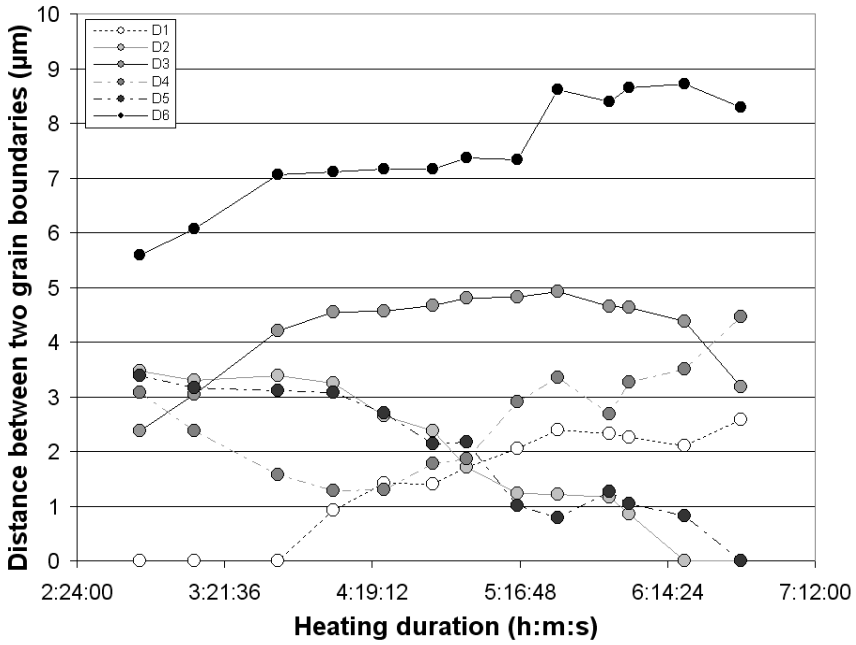

(a)

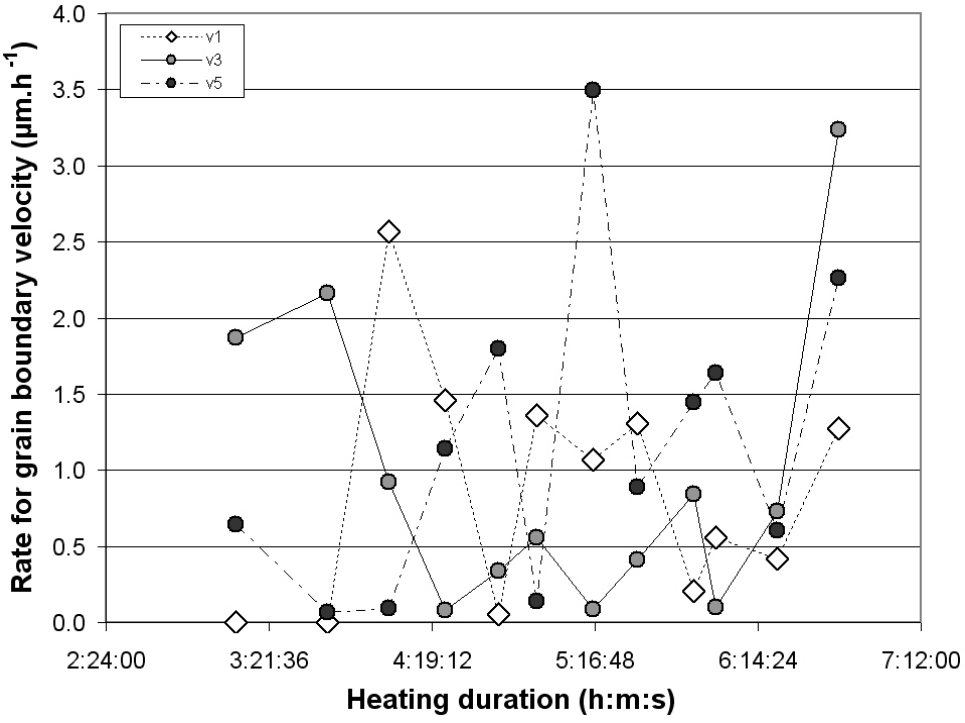

(b)

Figure 6 – Determination of the grain boundary velocity (a) Distances between two grains boundaries of a grain. (b) Instantaneous grain boundary velocity (only selected data are reported for easier reading)

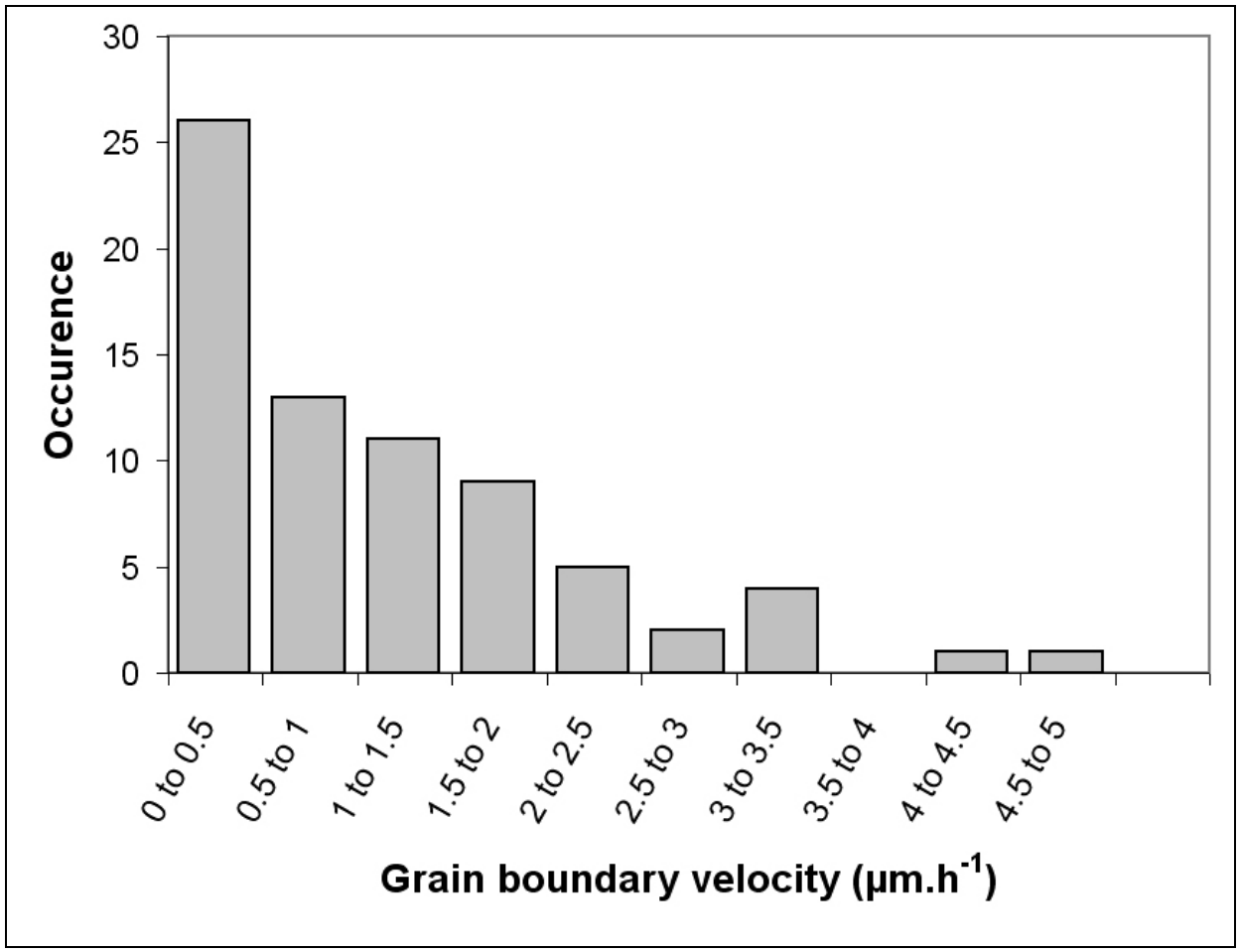

Figure 7 – Distribution of the grain boundary velocity for CeO_2 at T=1400°C

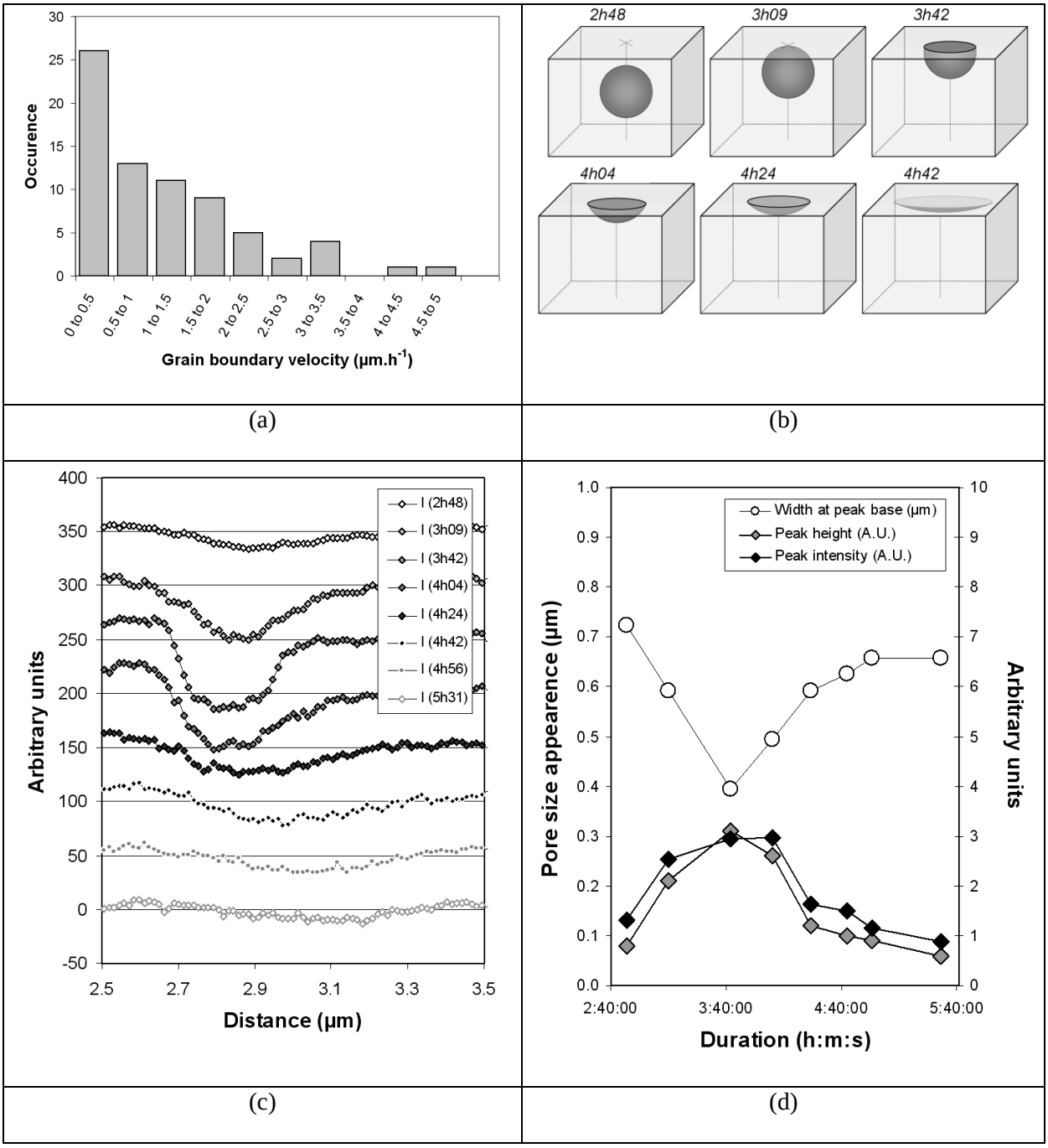

Figure 8 –(a) Pore images extracted from HT-ESEM series recorded at T=1400°C (view of the sample surface). (b) Intra granular pore trajectory from the bulk to the surface of the grain showing the pore elimination. (c) Grey levels expressed in arbitrary units extracted from pore images reported on (a). (d) Parameters used to characterize the pore morphology.

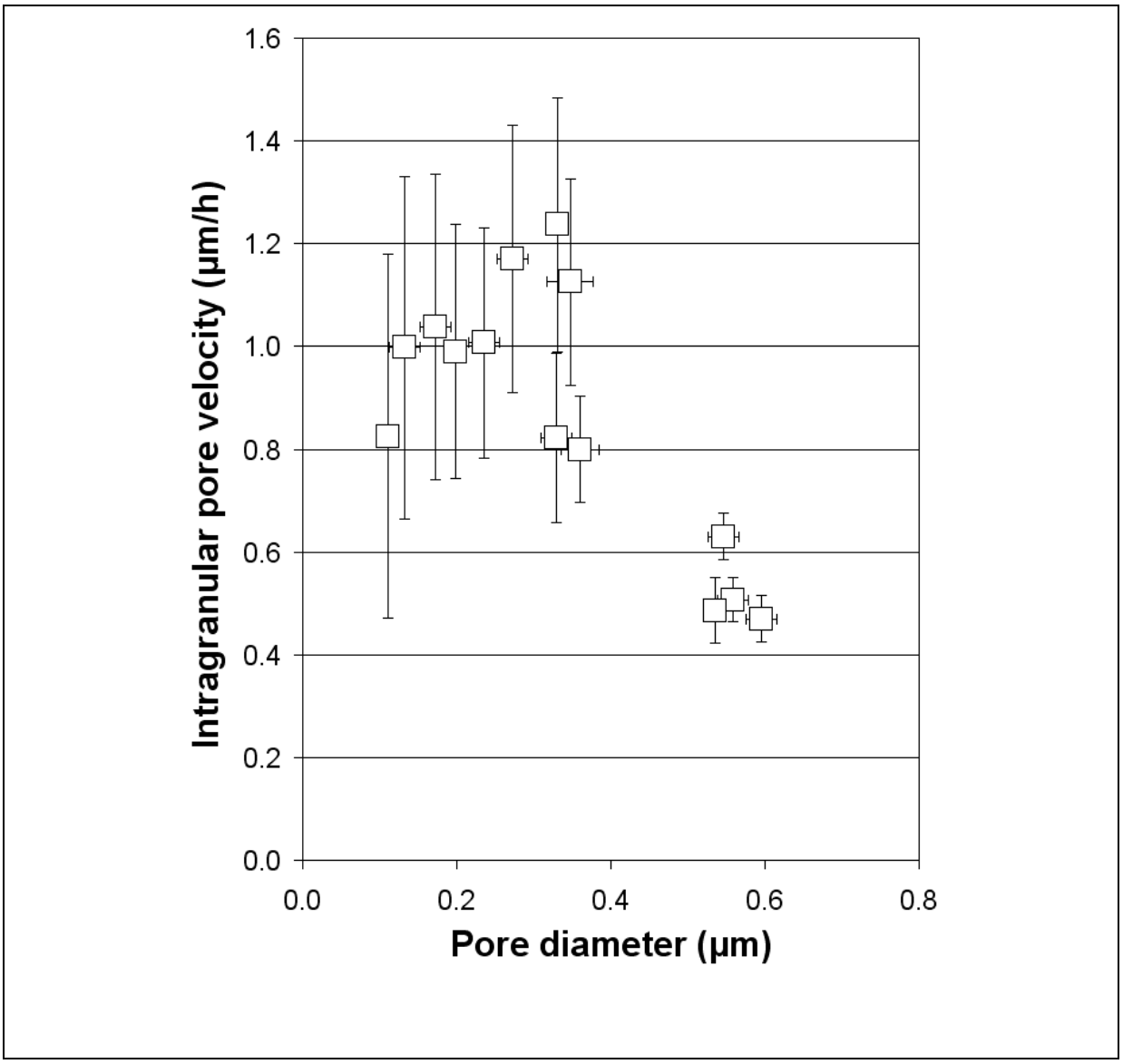

Figure 9 – Velocity of intra granular pore reported as a function of the pore diameter.

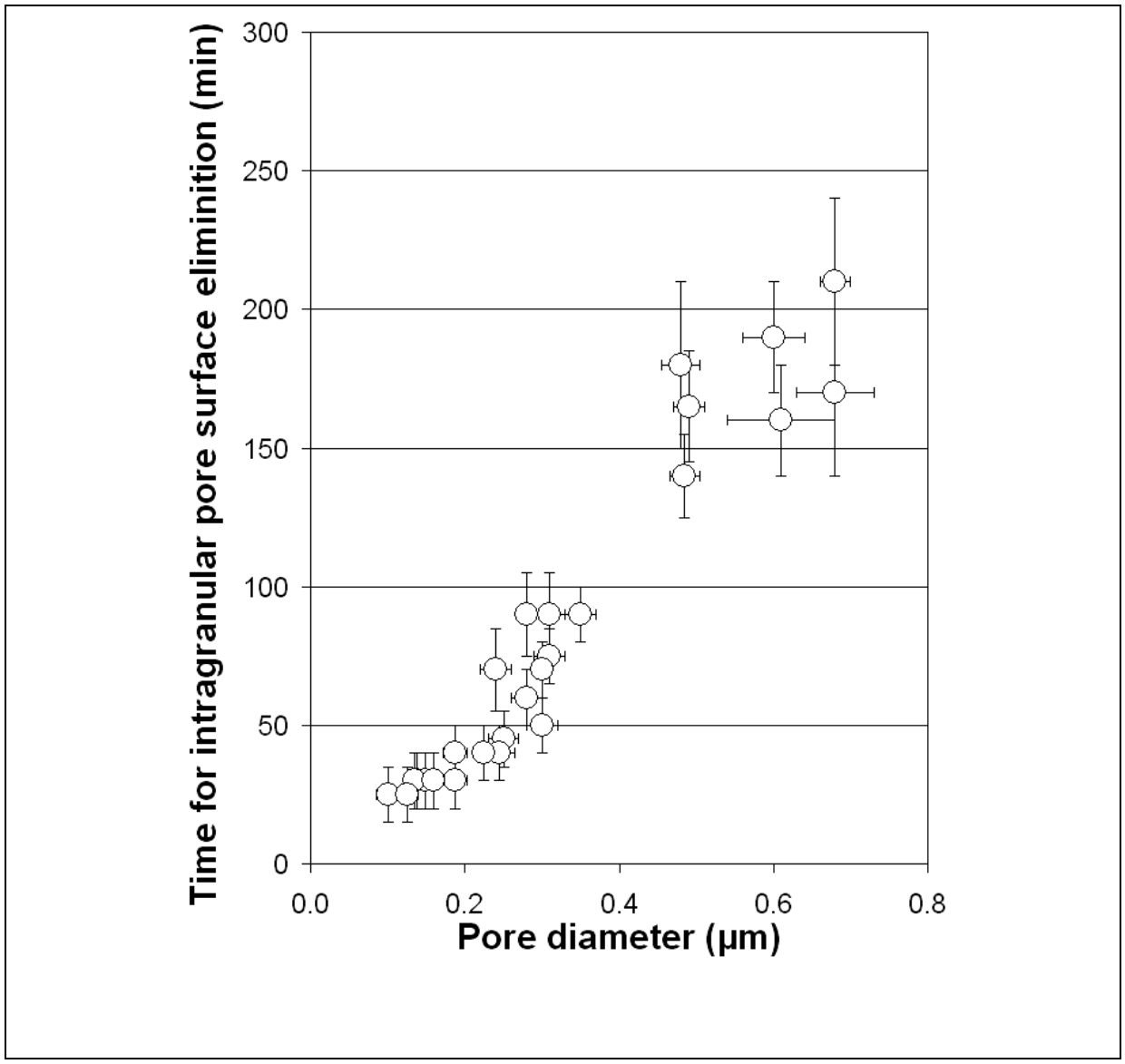

Figure 10 – Variations of the time required for the intragranular porosity elimination at the surface *versus* the pore diameter.